

QCD Anderson transition with overlap valence quarks on a twisted-mass sea

Robin Kehr,¹ Dominik Smith,^{1,2} and Lorenz von Smekal^{1,3}

¹*Institut für Theoretische Physik, Justus-Liebig-Universität, Heinrich-Buff-Ring 16, 35392 Giessen, Germany*

²*Facility for Antiproton and Ion Research in Europe GmbH (FAIR GmbH), 64291 Darmstadt, Germany*

³*Helmholtz Forschungsakademie Hessen für FAIR (HFHF), GSI Helmholtzzentrum für Schwerionenforschung, Campus Gießen*

In this work we probe the QCD Anderson transition by studying spectral distributions of the massless overlap operator on gauge configurations created by the *twisted mass at finite temperature collaboration* (tmfT) with 2+1+1 flavors of dynamical quarks and the Iwasaki gauge action. We assess finite-size and discretization effects by considering two different lattice spacings and several physical volumes, and mimic the approach to the continuum limit through stereographic projection. Fitting the inflection points of the participation ratios of the overlap Dirac eigenmodes, we obtain estimates of the temperature dependence of the mobility edge, below which quark modes are localized. We observe that it is well-described by a quadratic polynomial and systematically vanishes at temperatures below the pseudo-critical one of the chiral transition. In fact, our best estimates within errors overlap with that of the chiral phase transition temperature of QCD in the chiral limit.

I. INTRODUCTION

In his seminal paper titled “Absence of Diffusion in Certain Random Lattices” [1], P. W. Anderson studied non-interacting electrons in a disordered crystal using a tight-binding model with a random on-site potential. It was observed that a metal-insulator transition occurs, characterized by a vanishing of the zero-temperature conductivity, when the amplitude of the random source term exceeds a specific value. It was understood that the random potential creates a localization effect, such that low-lying electron eigenmodes exhibit an exponential decay in space due to destructive interference [2, 3]. At the transition point an energy threshold emerges, known as the *mobility edge*, which separates the spectrum of the Hamilton operator into localized and delocalized regimes. This is known as *Anderson localization* and has no classical analogon.

An intriguing idea, which by now is supported by strong numerical evidence, is that a similar transition occurs in finite-temperature QCD and other QCD-like theories, whereby eigenstates of the Dirac operator play the role of the electron modes. In lattice gauge theory this has been extensively studied, beginning with SU(2) gauge theory [4–7], as well as in three-color QCD, quenched [8–10] and unquenched [7, 11–16]. In each case, the spectrum of the Dirac operator exhibits a localized and a delocalized regime at high-temperatures, separated by a mobility edge λ_c . In quenched QCD, Anderson localization coincides with the deconfining phase transition [8–10] whereas in full QCD it appears at the chiral transition [14]. This suggests a close relationship between the three phenomena and implies that temperature plays a similar role as the disorder parameter in Anderson’s model [17].

For a recent review on localization in gauge theories, see [18]. Numerical evidence for the localization of low-lying Dirac modes preferentially in regions where disorder emerges in the Polyakov loop was given in [19–22]. The connection between localized near-zero modes and the possible existence of massless single-particle Goldstone

excitations in the chiral limit is discussed in detail in [23]. The overall picture emerging is that an accumulation of possibly localized near-zero modes, as observed right above the pseudo-critical temperature in lattice QCD with physical and smaller than physical light-quark masses [24–26], in the chiral limit might delocalize to produce chiral condensate and Goldstone pions with vanishing mobility edge right at the chiral phase transition. The disappearance of the mobility edge and Anderson localization at the chiral phase transition in QCD can therefore in principle provide no less than the connection between chiral symmetry restoration and deconfinement.

In this work, we study the spectrum and eigenmodes of the massless overlap operator, which exactly fulfills the Ginsparg-Wilson relation, on the background of SU(3) gauge field configurations generated by the *twisted mass at finite temperature collaboration* (tmfT) [27–29] with $N_f = 2+1+1$ flavors of twisted mass Wilson quarks at maximal twist and using the Iwasaki gauge action. Such a mixed-action setup was first proposed in Refs. [30, 31] where its feasibility was demonstrated. The first use of such a setup to investigate Anderson localization was reported in Ref. [21]. Our present study improves upon the previous one by considering larger physical volumes and smaller lattice spacings. The focus is a more precise determination of the temperature dependence of the mobility edge, using the inverse participation ratio of Dirac eigenmodes.

Some earlier works have reported an approximately linear dependence $\lambda_c(T) \approx c(T - T_0)$ [14, 21]. Here, we observe that a quadratic contribution can be extracted when the effects of the lattice spacing and volume and of unphysically large bare quark-masses are controlled. Using a stereographic projection of eigenvalues from the Ginsparg-Wilson circle to the imaginary axis to mimic the continuum limit, we then obtain evidence that the mobility edge vanishes very close to current estimates of the critical temperature of the chiral phase transition in the $m_q \rightarrow 0$ limit. This contrasts with previous studies, which have placed the Anderson transition closer to the pseudocritical temperature, i.e. in the proximity of the $m_q \neq 0$ crossover.

This work is structured as follows: We start by describing our lattice setup in detail in Sec. II, including a comprehensive list of the lattice configuration which were analyzed. In Sec. III we then describe our target observables, namely the distribution of eigenvalues and the inverse participation ratio, and our methods for obtaining them. We present results in Sec. IV. This includes the raw eigenvalue spectrum to illustrate the formation of a Banks-Casher gap, as well as our study of the temperature dependence of the mobility edge. The section is split into two parts: We first discuss the dependence of all observables on the polar angle of the Ginsparg-Wilson circle, and then in terms of the purely imaginary eigenvalues after stereographic projection. We summarize and conclude in Sec. V.

II. LATTICE SETUP

In this work, we use lattice configurations created by the *twisted mass at finite temperature collaboration* under guidance of the late Michael Müller-Preussker [27–29]. The ensembles were generated with $N_f = 2 + 1 + 1$ dynamical flavors of twisted mass Wilson quarks at maximal twist [32], with two degenerate light fermions, two non-degenerate heavy fermions, and the Iwasaki gauge action. These configurations are a subset of the ones presented in Ref. [33] and are listed comprehensively in Table I. We adopt the nomenclature of Ref. [33], as well as the physical values of the pion mass, lattice spacing and pseudocritical temperatures listed therein. The scale setting and tuning of the twist parameter is based on earlier work by Ref. [34] as well as zero-temperature simulations by the *European twisted mass collaboration* (ETMC) [35–38].

We employ a fixed scale approach. Our spectral computations were performed on three sets of ensembles (denoted by A370, D370 and D210) with two different lattice spacings, for several temperatures fixed by N_t . While strange and charm quarks have physical masses, the pion mass is still unphysically large in the ensembles considered here, with $m_\pi = 364(15)$ MeV, $m_\pi = 369(15)$ MeV and $m_\pi = 213(9)$ MeV, respectively. The chiral crossover occurs at $T_{pc} \approx 185$ MeV for larger pion masses and at $T_{pc} = 158(5)$ MeV for the smaller one. The physical sizes L of the spatial volumes are such that $m_\pi L \approx 4.14$ (A370), 3.86 (D370), and 3.34 (D210). Therefore, relative to the Compton wavelength of the pion the physical volume in the D210 ensemble is at the lower end and residual finite volume effects are to be expected, although with $N_s = 48$ the largest spatial lattice size was used in this case.

For our measurements we employ the overlap Dirac operator [39–42]. In particular, we study the spectrum and eigenmodes of the massless overlap operator

$$D = \frac{1}{a} (1 + \text{sgn } K) , \quad (1)$$

which exactly fulfills the Ginsparg-Wilson relation $\{\gamma_5, D\} = aD\gamma_5D$ [43, 44], where a is the lattice spacing.

Set of ensembles	N_s	N_t	T / MeV	T/T_{pc}	# conf.	$\frac{\text{modes}}{\text{conf.}}$	
A370 $a = 0.0936(13)$ fm $m_\pi = 364(15)$ MeV $T_{pc} = 185(8)$ MeV	24	4	527(7)	2.85(13)	200	200	
		5	422(6)	2.28(10)	200	160	
		6	351(5)	1.90(9)	200	135	
		7	301(4)	1.63(7)	150	115	
		8	264(4)	1.42(6)	200	100	
		9	234(3)	1.27(6)	200	90	
		10	211(3)	1.14(5)	250	80	
		11	192(3)	1.04(5)	200	75	
D370 $a = 0.0646(7)$ fm $m_\pi = 369(15)$ MeV $T_{pc} = 185(4)$ MeV	32	3	1018(11)	5.50(13)	120	400	
		6	509(6)	2.75(7)	120	200	
		14	218(2)	1.18(3)	160	85	
		16	191(2)	1.03(2)	160	75	
		40	18	170(2)	0.92(2)	20	150
		48	20	153(2)	0.83(2)	3	200
D210 $a = 0.0646(7)$ fm $m_\pi = 213(9)$ MeV $T_{pc} = 158(5)$ MeV	48	4	764(8)	4.83(16)	10	1000	
		6	509(6)	3.22(11)	10	700	
		8	382(4)	2.42(8)	10	500	
		10	305(3)	1.93(6)	10	400	
		12	255(3)	1.61(5)	10	350	

Table I. Overview of the tmfT ensembles used in this work, the number of configurations on which overlap eigenmodes were computed and the number of eigenmodes per configuration. Parameters and nomenclature adopted from Ref. [33] and [34]. Due to high computational costs, the computed eigenmodes for the D370 ensemble with $N_s = 48$ and $N_t = 20$ suffers from low statistics.

D obeys an Atiyah-Singer index theorem, implements the $U_A(1)$ anomaly on the lattice and is automatically $\mathcal{O}(a)$ improved [45, 46]. The sign function $\text{sgn } K = \frac{K}{\sqrt{K^\dagger K}}$ is computed using a rational (Zolotarev) approximation, while for the kernel K we used the Wilson operator with negative mass parameter $-\rho$ where $\rho \in (0, 2)$ is a scaling factor which can be tuned to optimize the locality properties of the overlap operator. We set it to $\rho = 1.4$ in this work as determined in Ref. [31] to be an optimal choice, if no additional smearing of the gauge fields is employed.

III. OBSERVABLES

A. Eigenvalue spectrum

The spectral density $\rho(\lambda)$ of a chiral Dirac operator can be related to the spontaneous breaking of chiral symmetry. The *Banks-Casher relation* [47–49] connects the near-zero spectral density of the Dirac operator with the chiral

condensate and reads

$$\langle \bar{\psi}\psi \rangle = -\pi \lim_{\lambda \rightarrow 0} \lim_{m \rightarrow 0} \lim_{V \rightarrow \infty} \rho(\lambda). \quad (2)$$

When chiral symmetry is broken, one hence finds $\langle \bar{\psi}\psi \rangle \propto \lim_{\lambda \rightarrow 0} \rho(\lambda) > 0$, while a restored chiral symmetry is reflected in $\lim_{\lambda \rightarrow 0} \rho(\lambda) = 0$ (more precisely, for the density of bulk modes, i.e. not including the possible near-zero modes of lower effective infrared dimension in the putative infrared phase of QCD above the chiral transition [50]). This implies that a gap opens in the spectral density of the Dirac operator above T_{pc} . At high temperatures, and at sufficient distance from the edge of the gap, the spectral density of eigenstates shows an approximate square root behavior [51].

The eigenmodes and eigenvalues of the massless overlap operator are the primary target of this study. To diagonalize the overlap operator, we use the *Krylov-Schur method* [52], as provided by the SLEPc library [53]. In previous work [21], the *implicitly restarted Arnoldi method* (IRAM) provided by the ARPACK library was employed instead [54, 55]. However, it was found that the Krylov-Schur method yields a significantly better performance, which was tested for one configuration per N_t of the D210 data set. Additionally, we noticed that one has to be careful using the ARPACK++ library [56], which provides a C++ interface to ARPACK with 32-bit integers, since integer overflows can occur for large scale diagonalizations, as done for this work.¹

In the continuum, the Dirac eigenvalues are purely imaginary, but on the lattice the overlap eigenvalues λ are distributed on the Ginsparg-Wilson circle with radius $1/a$, given by

$$\text{Im } \lambda = \pm \sqrt{\frac{2}{a} \text{Re } \lambda - (\text{Re } \lambda)^2}. \quad (3)$$

The continuum limit $a \rightarrow 0$ can be mimicked by stereographically projecting the eigenvalues onto the imaginary axis (see Fig. 1). In this work, we first present a discussion of the raw complex eigenvalues in terms of the polar angle

$$\varphi = \arctan\left(\frac{\text{Im } \lambda}{a^{-1} - \text{Re } \lambda}\right) \quad (4)$$

on the Ginsparg-Wilson circle. We then repeat the analysis with the projection applied for all data sets.

B. Inverse participation ratio

To probe and quantify localization, we use the relative space-time volume $r(\lambda)$ that is occupied by an eigenmode.

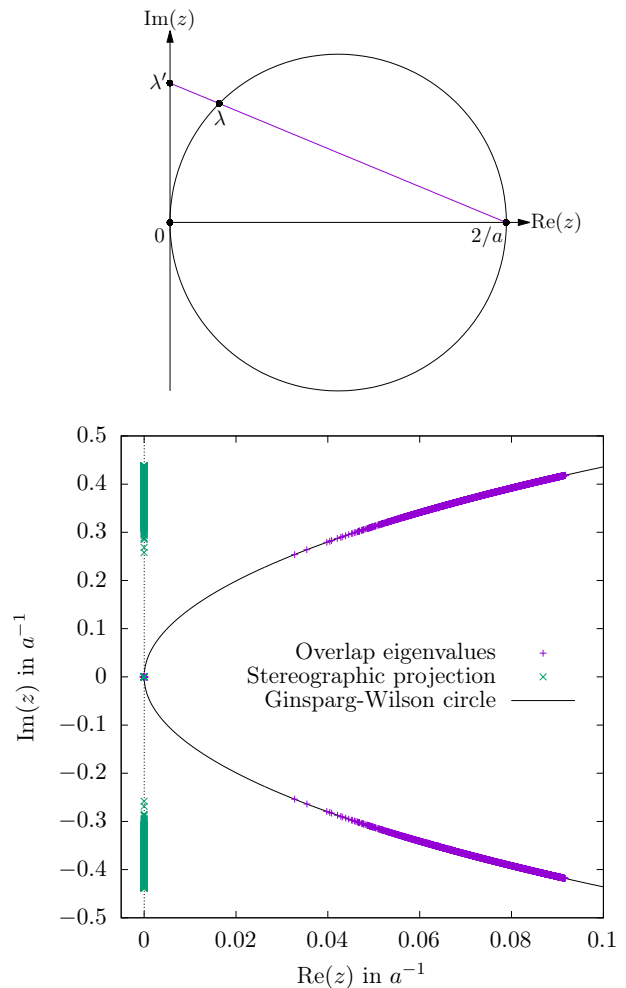


Figure 1. *Top*: Stereographic projection of the eigenvalues at finite a to the imaginary axis. *Bottom*: Projection of eigenvalues at $T = 509.10(5.52)$ MeV for the D210 data set.

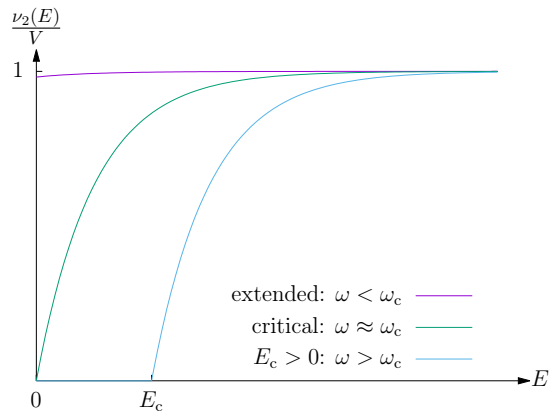


Figure 2. A sketch of the normalized electron participation ratio $\nu_2(E)/V$ over the energy E for disorder terms ω below, close to and above the Anderson transition.

¹ The SLEPc library, on the other hand, can be installed with a 64-bit integer option and contains such an interface as well.

This relative volume or participation ratio $r(\lambda)$ is computed using the inverse participation ratio (IPR), see, e.g., Refs. [11, 16]. The j -th order (generalized) IPR of an eigenmode v_λ is defined as

$$\nu_j^{-1} = \sum_{n \in \Lambda} (v_\lambda(n)^\dagger v_\lambda(n))^j, \quad (5)$$

where the sum runs over all sites n of the 4D lattice Λ . A maximally localized mode only occupies one lattice site, so $v_\lambda(n)^\dagger v_\lambda(n) = \delta_{n,n'}$, which implies $\nu_j = 1$. A maximally extended and hence homogeneously distributed eigenmode with $v_\lambda(n)^\dagger v_\lambda(n) = 1/|\Lambda|$ yields $\nu_j = |\Lambda|^{j-1}$.

Since the second order participation ratio ν_2 is by definition proportional to the volume that the eigenmode occupies, one can define the relative eigenmode volume

$$r(\lambda) = \frac{\nu_2(\lambda)}{|\Lambda|} \in [1/|\Lambda|, 1], \quad (6)$$

where $r(\lambda) = 1/|\Lambda|$ and $r(\lambda) = 1$ correspond to fully localized and delocalized modes, respectively. In practice the eigenvalues are discrete, and r scatters even for nearby values of λ , so we average $r(\lambda)$ over small bins of size $\Delta\lambda$ to approximate a smooth function. We define λ_c as the spectral position of the inflection point of the bin-averaged relative participation ratio $\overline{r(\lambda)}$.

The normalized participation ratio $\nu_2(E)/V$ in the original Anderson model, of electron modes at energy E in the volume V , is sketched in Fig. 2. Qualitatively, this picture equally applies to each of the different variants of the model, with different symmetry groups.

IV. RESULTS

A. Angular dependence

We start by discussing the Anderson transition in terms of the polar angle φ of the complex eigenvalues of the overlap operator, which are distributed on the Ginsparg-Wilson circle. Since the eigenvalues come in complex conjugate pairs with equal relative volume, it is sufficient to regard the absolute value of the eigenvalues. For better readability, we redefine $\varphi := |\varphi|$ and $r(\varphi) := \overline{r(\varphi)}$ in the following discussion. In Figs. 3, 4 and 5 we show histograms with binsize $\Delta\varphi = 2.5 \cdot 10^{-3}$, which estimate the angle-dependent eigenvalue probability density $\rho(\varphi)$ for the A370, D370 and D210 data set for different temperatures.

The chiral transition occurs at $T_{pc} \approx 185$ MeV (for the A370 and D370 data set) and at $T_{pc} \approx 158$ MeV (D210) respectively (see Table I); most of the presented temperatures are thus in the chirally symmetric phase. We clearly observe the Banks-Casher gap, which grows as the temperature increases. Due to finite volume and discretization effects, there are still eigenmodes within the Banks-Casher gap at small temperatures (close to T_{pc}); it

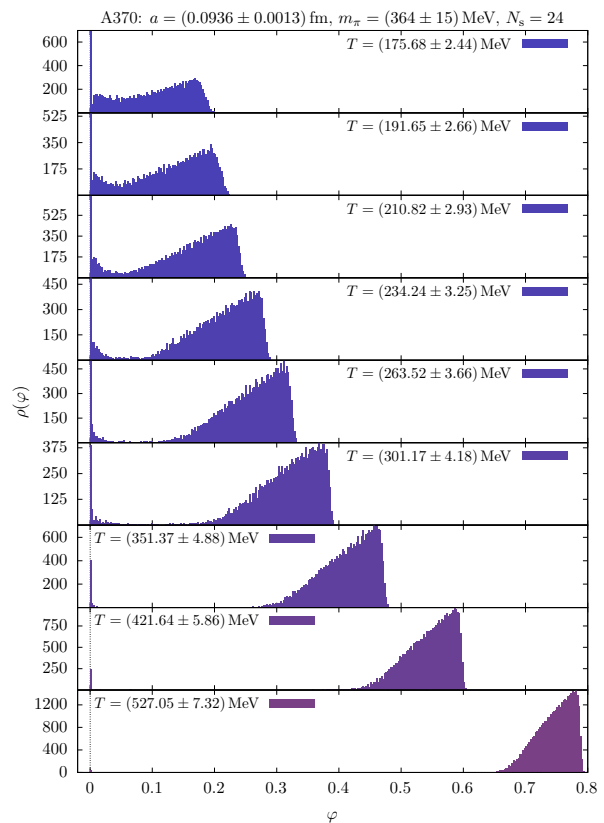


Figure 3. Angular distribution of overlap eigenvalues for A370 configurations ($a = 0.0936(13)$ fm; $m_\pi = 364(15)$ MeV).

has not fully opened. Also, each ensemble contains zero modes which are eigenvectors of γ_5 and hence chiral.

In Figs. 6, 7 and 8 the relative eigenmode volume $r(\varphi)$ is shown for each data set. We estimate the mobility edge by determining the inflection points φ_c , hence

$$\left. \frac{\partial^2 r(\varphi)}{\partial \varphi^2} \right|_{\varphi=\varphi_c} = 0, \quad (7)$$

using fits of the form

$$r(\varphi) = r_c + b(\varphi - \varphi_c) + c(\varphi - \varphi_c)^3 + d(\varphi - \varphi_c)^4. \quad (8)$$

To maximize the goodness of fit of our model, aside from the fit constants r_c , φ_c , b , c , d , we vary the lower (left) and upper (right) bounds of the fit-window φ_l and φ_r , and the binsize $\Delta\varphi$ over which $r(\varphi)$ is averaged. In doing so, we obtain fits where the reduced χ ($= \sqrt{\chi^2/\text{d.o.f.}}$) is unity to at least two digits precision for most of the data sets. The optimized binsize and boundaries as well as the reduced χ are given in boxes as part of the legend in each figure. The corresponding fit windows are furthermore indicated by vertical red lines, and the resulting inflection points φ_c as red circles (with errorbars). With the single exception of the lowest temperature in the A370 ensemble (where a value consistent with zero is obtained for φ_c), the inflection point always falls well inside the fit window.

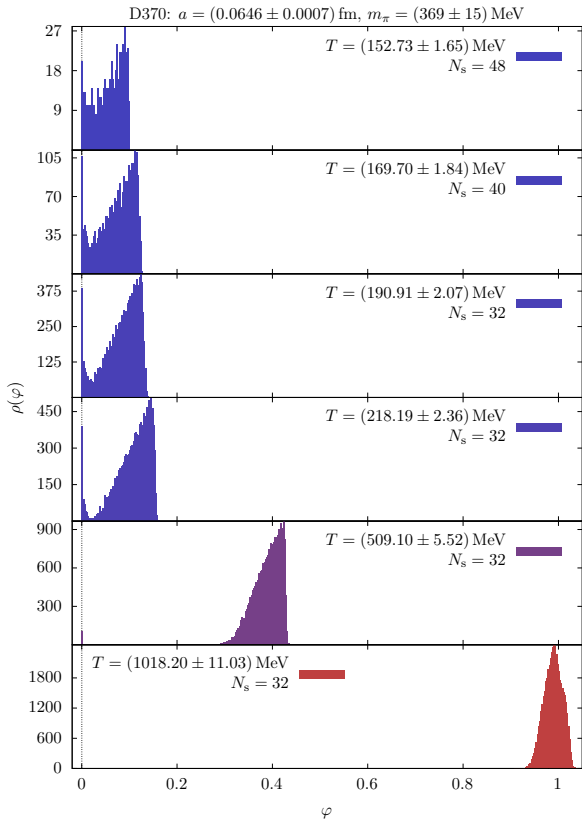


Figure 4. Angular distribution of overlap eigenvalues for D370 configurations ($a = 0.0646(7)$ fm; $m_\pi = 369(15)$ MeV).

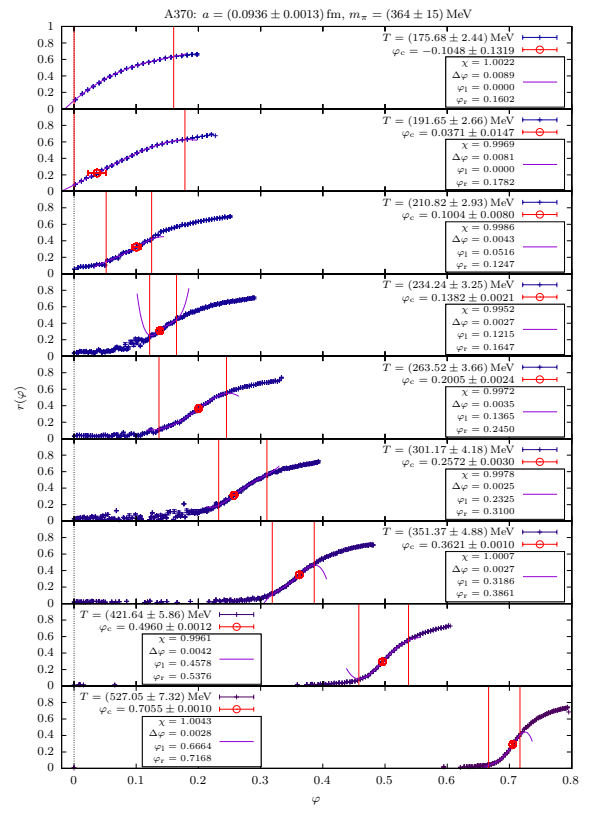


Figure 6. Angular dependence of relative eigenmode volume $r(\varphi)$ for A370 configurations.

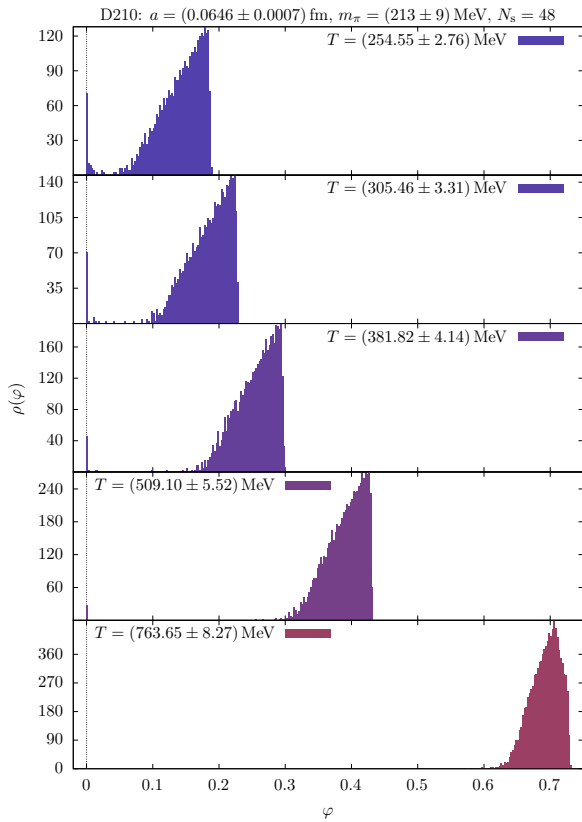


Figure 5. Angular distribution of overlap eigenvalues for D210 configurations ($a = 0.0646(7)$ fm; $m_\pi = 213(9)$ MeV).

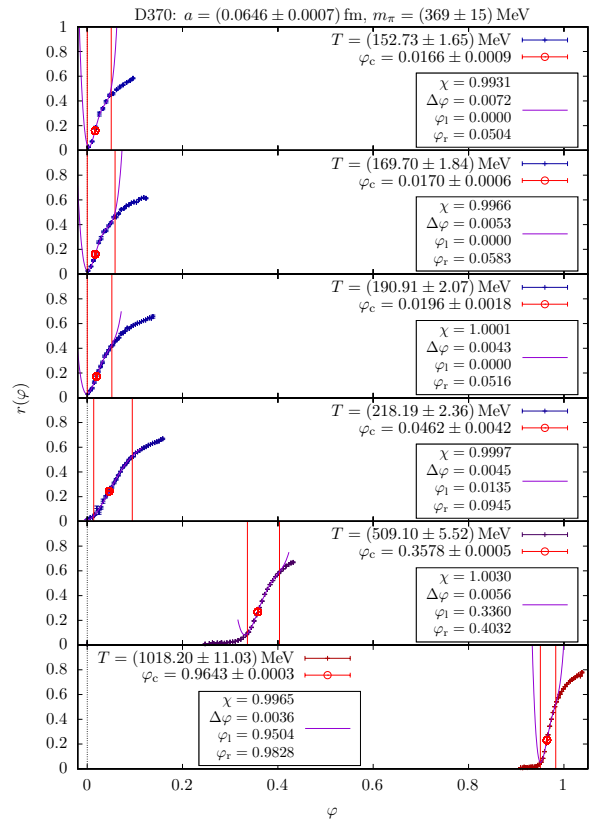


Figure 7. Angular dependence of relative eigenmode volume $r(\varphi)$ for D370 configurations.

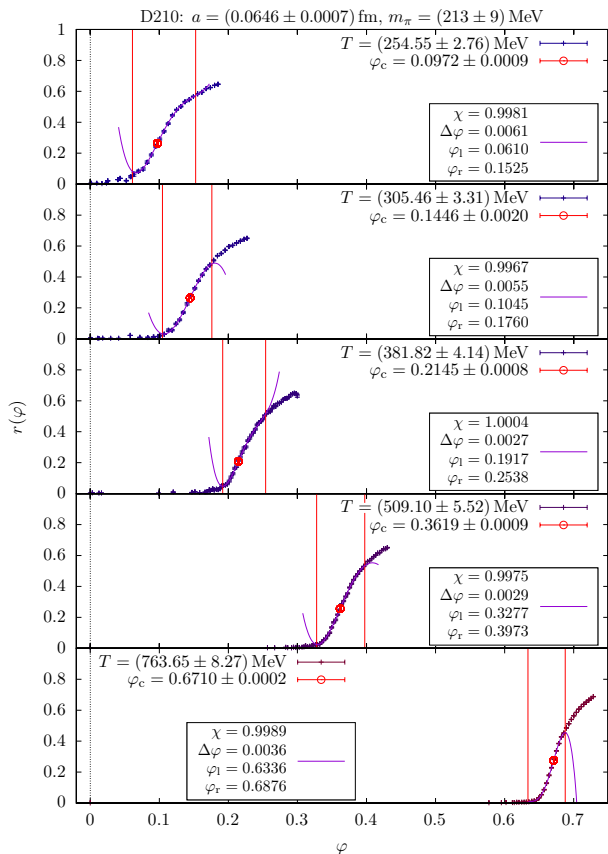


Figure 8. Angular dependence of relative eigenmode volume $r(\varphi)$ for D210 configurations.

In fact, the pertinent fits are of such quality that they are hard to distinguish from the data inside the fit windows in our figures. For better visibility, we have therefore plotted these fits slightly beyond the respective windows used to obtain them. The so obtained values of the inflection points φ_c as our final estimates of the mobility edge are listed in Table II.

We then use these values to estimate the Anderson transition temperature T_0 , where the mobility edge vanishes, applying fits of the form

$$\varphi_c(T) = b(T - T_0)^2 + c(T - T_0), \quad (9)$$

to all data sets. We thereby use the uncertainties in the lattice spacings to obtain error bars in T , which we then apply to all data points in the fitting procedure. The resulting curves are shown in Fig. 9 together with the raw data $\varphi_c(T)$ obtained from the inflection points for the A370 (top), D370 (middle) and D210 (bottom) ensembles, respectively. Our estimates of T_0 , where $\varphi_c = 0$, are indicated by red circles together with the fit error bars (which hardly exceed the symbol size) in these plots.

The temperature dependence of the mobility edge from the coarse and small lattice with heavier pion mass used for the A370 ensemble is approximately linear as observed previously [21]. For the D370 data set we find values of

$\chi \ll 1$, indicating over-fitting, which is likely due to the comparatively small number of data points: The two sets of configurations with $N_t = 18$ and 20, which are listed as part of the D370 data set in Table I, have larger N_s values (hence larger physical volumes) and were excluded from the fit, thus leaving only four data points for a three parameter fit. Displayed separately in the figures, the values of φ_c for these two data sets from the larger spatial volumes do indicate, however, that T_0 will tend to values smaller than the extrapolated one from the fit (indicated by the red circle) when the volume is increased.

While this suggests that a linear model would suffice to describe the rather sparse data (from the same volume) in this case as well, the quadratic term is certainly necessary for the D210 data set, on the other hand. In comparison, this data set is the most important one, however, because it has the largest physical volume, smallest lattice spacing and closest to physical pion mass, anyway. With these most realistic lattice parameters, the curvature is then clearly visible in the bottom plot of Figure 9.

Moreover, it is important to note here, that in all cases we obtain T_0 estimates which fall just outside (in particular below) the error bands of the pseudo-critical temperatures T_{pc} as determined for the chiral crossover transition in Ref. [33] with these ensembles, and indicated together with their respective error bands by the vertical dashed lines labeled T_{pc} in these figures. For comparison, we have also included the most recent estimate of the critical temperature T_c of the chiral phase transition (for $m_q \rightarrow 0$) taken from Ref. [57] in the same way. Incidentally, in the D210 case, we find that our T_0 error bar slightly overlaps with the T_c error band for the chiral phase transition temperature.

B. Stereographic projection

As a means of estimating, at least qualitatively, the effect of continuum extrapolations, we apply the stereographic projection sketched in Fig. 1, from the Ginsparg-Wilson circle onto the imaginary axis, to the eigenvalues for all data sets, i.e. we define the pure imaginary quantity

$$\lambda' := \frac{i \operatorname{Im} \lambda}{1 - \frac{g}{2} \operatorname{Re} \lambda}, \quad (10)$$

and repeat the investigation of the last section in terms of this new variable. Again, we redefine $\lambda := |\lambda'|$ and $r(\lambda) := \overline{r(\lambda')}$ for better readability.

Following the same steps as before, we start with illustrating the raw eigenvalue spectrum of $\rho(\lambda)$ for all data sets in Figs. 10, 11 and 12, using histograms with binsize $a\Delta\lambda = 2.5 \cdot 10^{-3}$. We show the corresponding relative eigenmode volume data in Figs. 13, 14 and 15, with fits, fit windows and resulting inflection points λ_c indicated in the same way as in Figs. 6, 7 and 8 above. Here we use fits of the form

$$r(\lambda) = r_c + b(\lambda - \lambda_c) + c(\lambda - \lambda_c)^3 + d(\lambda - \lambda_c)^4 \quad (11)$$

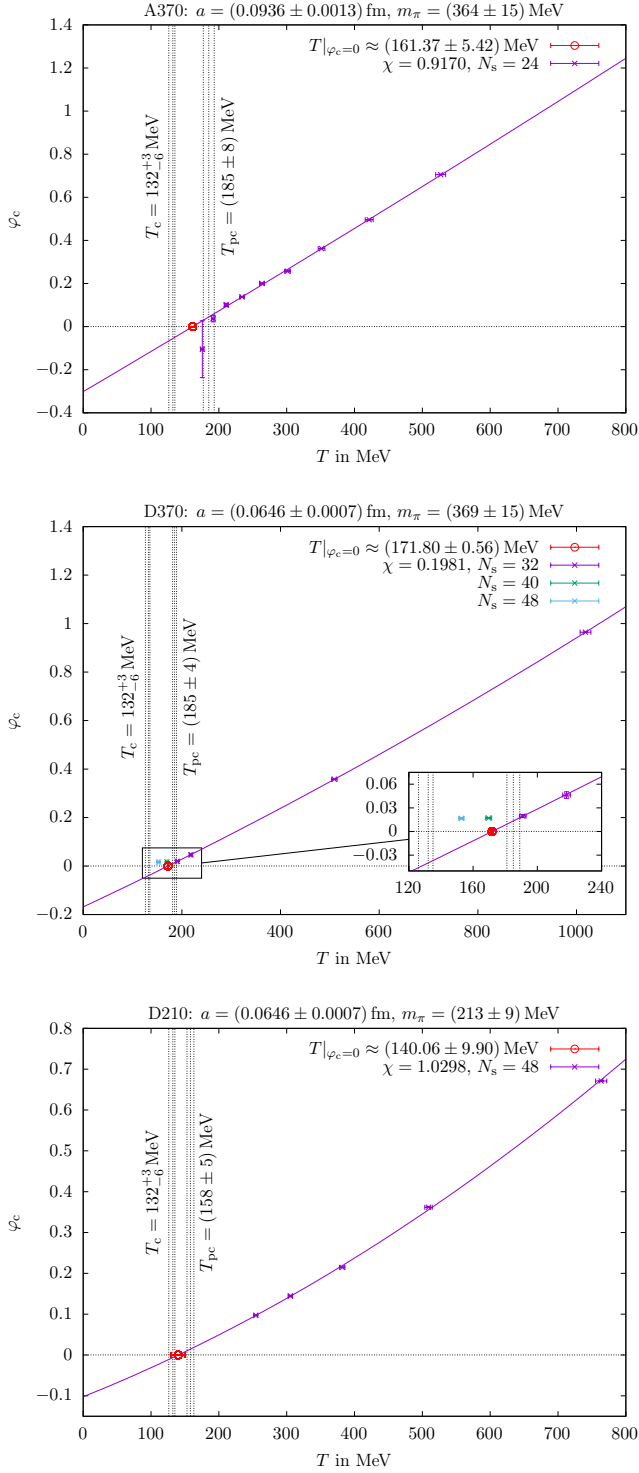


Figure 9. Temperature dependence of mobility edge for A370 (top), D370 (middle) and D210 (bottom) configurations, obtained from the angular eigenvalue distribution.

Set of ensembles	N_s	N_t	T / MeV	T/T_c	φ_c		
A370 $T_0 = 161(5) \text{ MeV}$	24	4	527(7)	2.85(13)	0.7055(10)		
		5	422(6)	2.28(10)	0.4960(12)		
		6	351(5)	1.90(9)	0.3621(10)		
		7	301(4)	1.63(7)	0.2572(30)		
		8	264(4)	1.42(6)	0.2005(24)		
		9	234(3)	1.27(6)	0.1382(21)		
		10	211(3)	1.14(5)	0.1004(80)		
		11	192(3)	1.04(5)	0.0371(147)		
		12	176(2)	0.95(4)	-0.1048(0.1319)		
		D370 $T_0 = 172(1) \text{ MeV}$	32	3	1018(11)	5.50(13)	0.9643(3)
				6	509(6)	2.75(7)	0.3578(5)
				14	218(2)	1.18(3)	0.0462(42)
16	191(2)			1.03(2)	0.0196(18)		
40	18		170(2)	0.92(2)	0.0170(6)		
48	20		153(2)	0.83(2)	0.0166(9)		
D210 $T_0 = 140(10) \text{ MeV}$	48	4	764(8)	4.83(16)	0.6710(2)		
		6	509(6)	3.22(11)	0.3619(9)		
		8	382(4)	2.42(8)	0.2145(8)		
		10	305(3)	1.93(6)	0.1446(20)		
		12	255(3)	1.61(5)	0.0972(9)		

Table II. Angular mobility edges determined from inflection points $\left. \frac{\partial^2 r(\varphi)}{\partial \varphi^2} \right|_{\varphi=\varphi_c} = 0$.

to obtain the mobility edges λ_c and again optimize the fit boundaries and binsizes for this purpose. Finally, we show the temperature dependence $\lambda_c(T)$ in Fig. 16, where we again apply fits of the form

$$\lambda_c(T) = b(T - T_0)^2 + c(T - T_0), \quad (12)$$

to obtain the Anderson transition temperatures T_0 . The corresponding numerical data is shown in Table III.

Comparing Figs. 9 and 16, the main observation here is that the projection appears to have a significant effect on the mobility edge only for the D210 data set. For A370 and D370, on the other hand, we find that the extrapolated T_0 values agree within errors with the non-projected results of the last section, and hence also fall just slightly below the pseudocritical temperatures T_{pc} for each case. In contrast, for the D210 ensemble, with the closest to physical pion mass (but smallest $m_\pi L \approx 3.34$), the T_0 prediction moves substantially, from 140(10) MeV down to 129(14) MeV, after applying the projection.

This new result then falls directly into the error band of $T_c = 132_{-6}^{+3} \text{ MeV}$ for the chiral phase transition temperature [57], but places the pseudocritical crossover temperature $T_{pc} = 158(5) \text{ MeV}$ at a distance of almost two standard deviations, see Fig. 16.

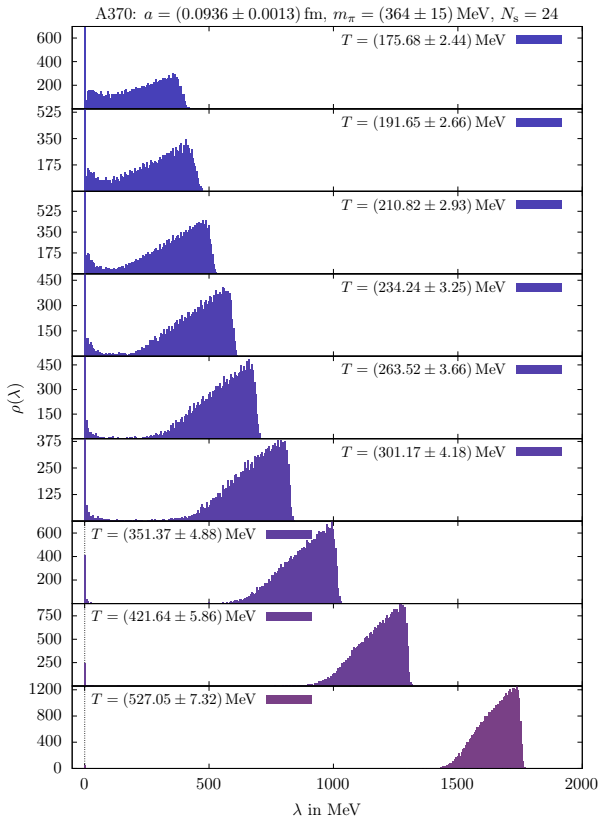


Figure 10. Distribution of projected overlap eigenvalues for A370 configurations ($a = 0.0936(13)$ fm; $m_\pi = 364(15)$ MeV).

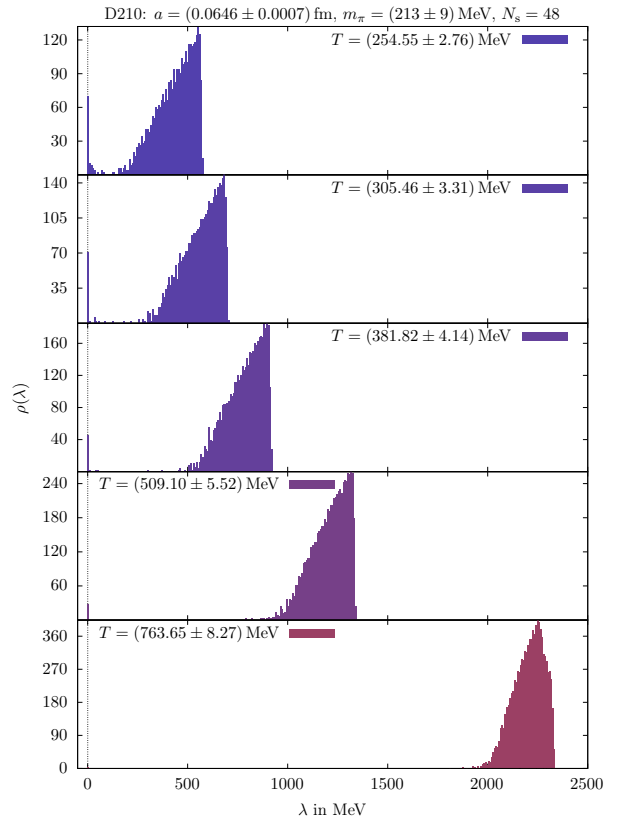


Figure 12. Distribution of projected overlap eigenvalues for D210 configurations ($a = 0.0646(7)$ fm; $m_\pi = 213(9)$ MeV).

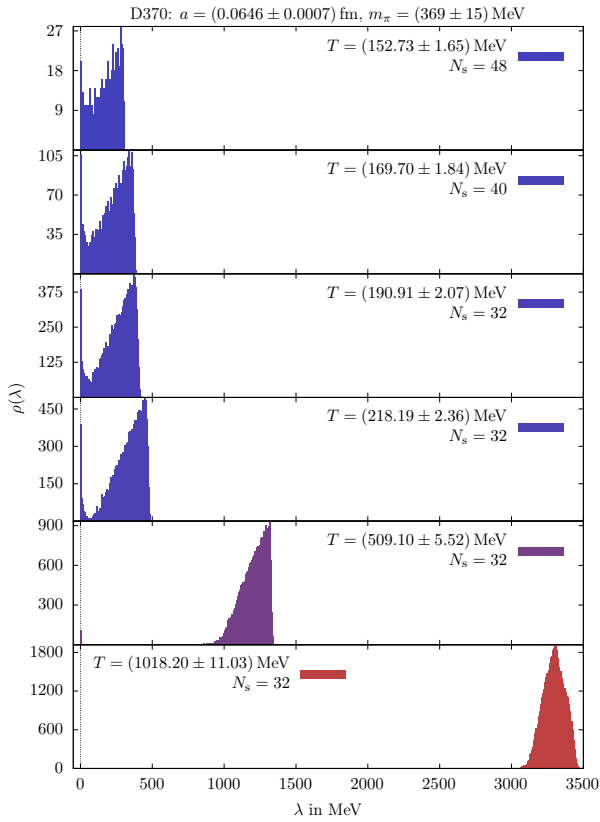


Figure 11. Distribution of projected overlap eigenvalues for D370 configurations ($a = 0.0646(7)$ fm; $m_\pi = 369(15)$ MeV).

V. CONCLUSION AND OUTLOOK

In this work, we have studied the spectral properties of the QCD overlap operator on SU(3) gauge field configurations created with dynamical twisted mass Wilson quarks and the Iwasaki gauge action, for several temperatures, with two different lattice spacings, two essentially different (physical) volumes and two different pion masses. After presenting the raw eigenvalue spectrum and demonstrating the formation of the Banks-Casher gap, we have extracted the relative volume that is occupied by eigenmodes from the inverse participation ratio across a broad spectral range, and obtained estimates for the mobility edge from the inflection points. We have finally discussed the temperature dependence of the mobility edge for all data sets.

While we have confirmed the linear T -dependence seen in earlier work for the configurations in smaller volumes with coarser lattice spacings and larger pion masses, we find that a quadratic contribution appears when moving towards the continuum limit and the physical point. This has been demonstrated with high statistical significance. Furthermore, when attempting to extrapolate the mobility edge to the chiral transition, we find that the Anderson transition temperature (where the mobility edge vanishes) consistently undershoots the chiral crossover temperature

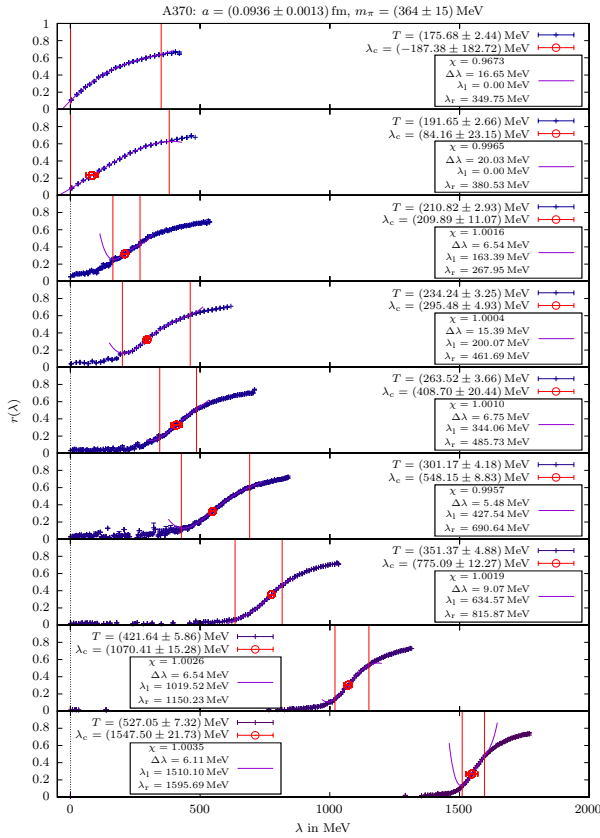


Figure 13. Relative eigenmode volume $r(\lambda)$ for A370 configurations.

predicted for the given value of the pion mass of each data set. This effect becomes more pronounced as lattice artifacts get under better control. For our best data set (with the largest physical volume, smallest lattice spacing and smallest pion mass), we find that the Anderson transition falls much closer to the predicted critical temperature of the chiral phase transition, in the limit of vanishing quark masses. In fact, we observe a nearly perfect coincidence, within statistical errors, after applying a stereographic projection of the eigenvalues to the imaginary axis, which mimics the continuum limit.

With the framework created for this project, there is a wide range of possible topics for future studies. At present, there are ongoing efforts to study the *unfolded level spacing distribution* (ULSD) for the different data sets. It is known that electron-mode delocalization is reflected in the ULSD for each of the different variants of Anderson's model, which are classified by the symmetries of the Hamiltonian [58]. The delocalized modes are thereby well-described with Wigner-Dyson random matrix theories (RMT) [59], while the level spacings for localized modes are Poisson distributed [6, 12].

QCD and related theories appear to follow a similar pattern: in the chirally broken phase, the entire Dirac operator spectrum follows RMT predictions [60, 61]. Different random matrix ensembles (each corresponding to a

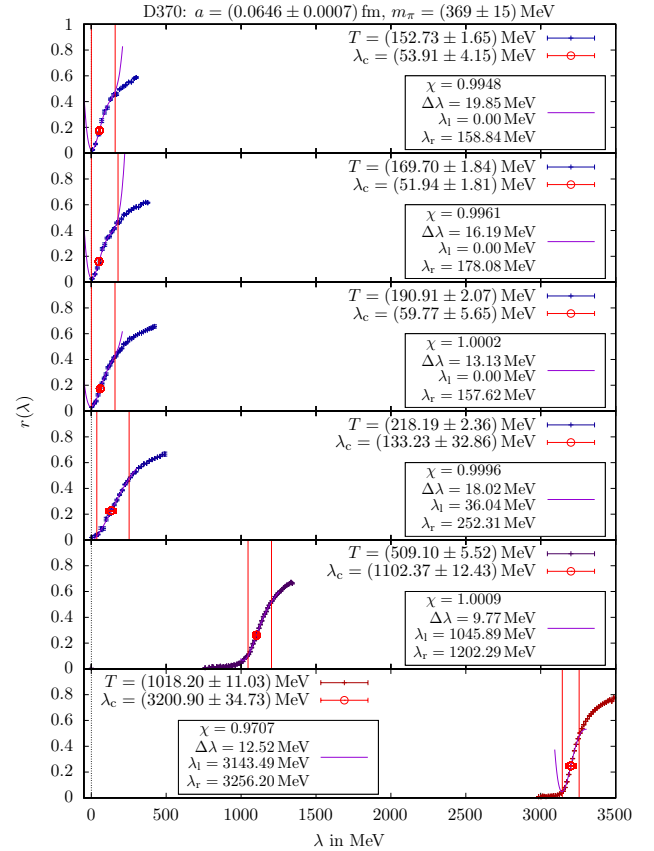


Figure 14. Relative eigenmode volume $r(\lambda)$ for D370 configurations.

different Anderson model) are thereby realized by different gauge-symmetry groups: the chiral Gaussian unitary ensemble (GUE) with Dyson-index $\beta_D = 2$ for three-color QCD [12]; the Gaussian orthogonal ensemble (GOE) with $\beta_D = 1$ for two-color QCD in the continuum [62]; the Gaussian symplectic ensemble (GSE) with $\beta_D = 4$ in any-color QCD with quarks in the adjoint representation [63], fundamental quarks in G_2 -QCD [64] or QC_2D with staggered quarks in the bulk phase [65, 66]. In the chirally restored phase the ULSD of localized ($\lambda < \lambda_c$) modes follows a Poisson distribution. This has been shown for both the GUE (through simulations of QCD with three colors e.g. in Ref. [12]) and the GSE (for staggered QC_2D e.g. in Ref. [6]). Using the same setup as in this work, it should be possible to study this effect with improved precision.

Also ongoing is a study of the effect of UV-smoothing the gauge configurations with gradient flow, in order to verify, e.g., that the anti-correlation between the Polyakov loop and the scalar density of eigenmodes, as discussed in several previous works [19–22], is preserved after smoothing. Local Polyakov loop fluctuations act similar to the random potential in Anderson's model and cause low energy wave functions to localize. This possibly connects

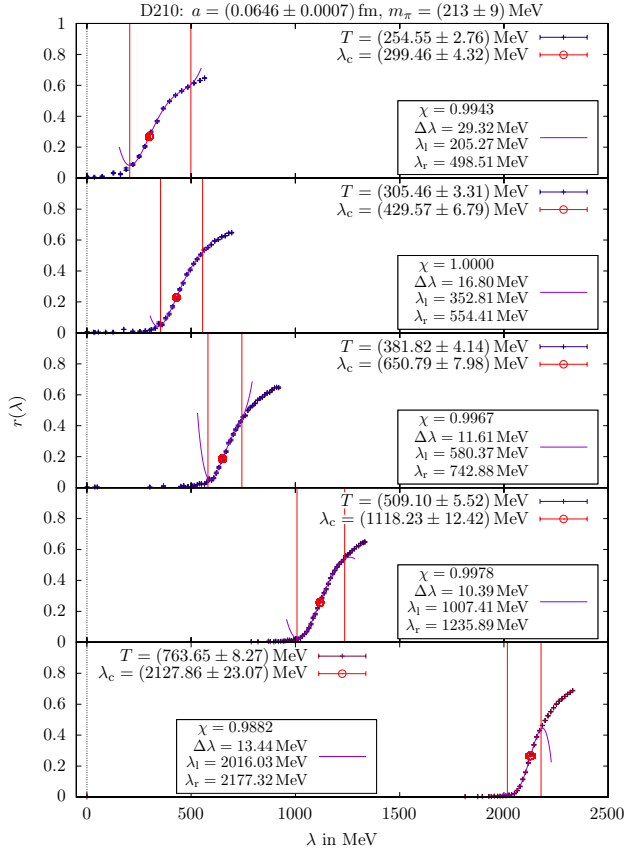


Figure 15. Relative eigenmode volume $r(\lambda)$ for D210 configurations.

deconfinement to the chiral transition.

Future studies might aim at shedding light on the connection between mode localization and the topological structure of QCD, i.e. by studying the topological charge density and its correlation to the scalar density of eigenmodes. Model studies have proposed that zero modes are bound to instantons and overlaps between neighboring instantons create a chiral condensate as the zero modes delocalize and obtain finite eigenvalues [67–69]. While the effectiveness of this mechanism has been questioned [8], this is possibly a driver of the Anderson transition in QCD. Instantons thereby act analogous to spatial regions with a low density of impurities, to which localized electron wave functions are bound.

Modes close to λ_c have also been shown to possess a multifractal structure in previous works [7, 15, 16], and the mobility edge was identified as a scale-invariant fixed point of the ULSD in QCD with two and three colors [7]. Both of these issues are of great interest, and deserve closer inspection.

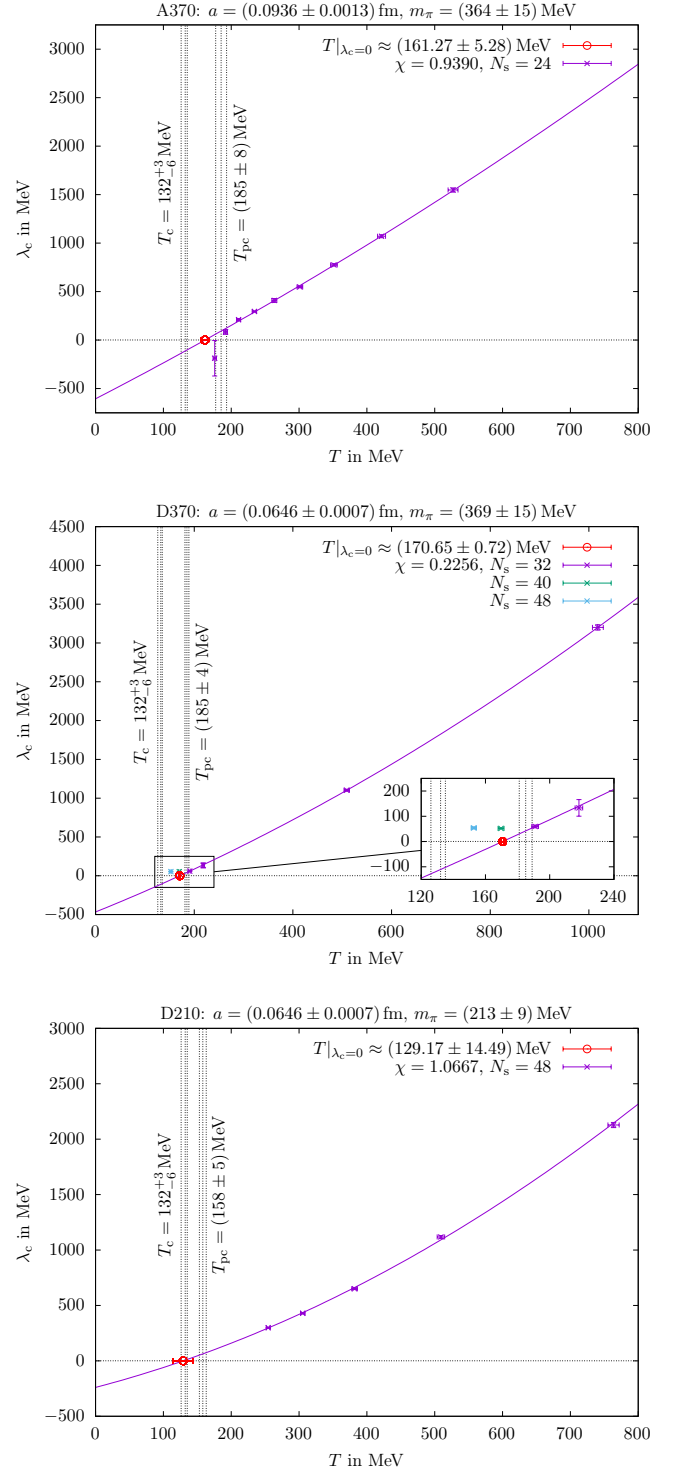


Figure 16. Temperature dependence of mobility edge for A370 (*top*), D370 (*middle*) and D210 (*bottom*) configurations, obtained by stereographic projection.

Set of ensembles	N_s	N_t	T / MeV	T/T_c	λ_c / MeV
A370 $T_0 = 161(5) \text{ MeV}$	24	4	527(7)	2.85(13)	1548(22)
		5	422(6)	2.28(10)	1070(15)
		6	351(5)	1.90(9)	775(12)
		7	301(4)	1.63(7)	548(9)
		8	264(4)	1.42(6)	409(20)
		9	234(3)	1.27(6)	295(5)
		10	211(3)	1.14(5)	210(11)
		11	192(3)	1.04(5)	84(23)
D370 $T_0 = 171(1) \text{ MeV}$	32	3	1018(11)	5.50(13)	3201(35)
		6	509(6)	2.75(7)	1102(12)
		14	218(2)	1.18(3)	133(33)
		16	191(2)	1.03(2)	60(6)
	40	18	170(2)	0.92(2)	52(2)
	48	20	153(2)	0.83(2)	54(4)
D210 $T_0 = 129(14) \text{ MeV}$	48	4	764(8)	4.83(16)	2128(23)
		6	509(6)	3.22(11)	1118(12)
		8	382(4)	2.42(8)	651(8)
		10	305(3)	1.93(6)	430(7)
		12	255(3)	1.61(5)	299(4)

Table III. Mobility edges determined from inflection points $\frac{\partial^2 r(\lambda)}{\partial \lambda^2} \Big|_{\lambda=\lambda_c} = 0$.

ACKNOWLEDGMENTS

D. S. received funding from the European Union’s Horizon 2020 research and innovation programme under grant agreement No. 871072. Early parts of this work were also supported by the Helmholtz International Center for FAIR within the LOEWE initiative of the State of Hesse. We thank Michael Ilgenfritz and Maria Paola Lombardo for many helpful discussions and for providing the tmfT configurations. We also thank Lukas Holicki for an implementation of the overlap Dirac operator. We also acknowledge helpful discussions with Matteo Giordano, Andrey Kotov, and Tamás Kovács. Computational resources were provided by the HPC Core Facility and the clusters of the Institute for Theoretical Physics with support of the HRZ of Justus-Liebig University Giessen.

-
- [1] P. W. Anderson, *Absence of diffusion in certain random lattices*, *Phys. Rev.* **109** (1958) 1492–1505.
- [2] P. Markos, *Absence of diffusion in certain random lattices: Numerical evidence*, *ArXiv e-prints* (July, 2008), [0807.2531].
- [3] J. Froehlich and T. Spencer, *A rigorous approach to anderson localization*, *Physics Reports* **103** (1984) 9 – 25.
- [4] F. Bruckmann, S. Keppeler, M. Panero and T. Wettig, *Polyakov loops and spectral properties of the staggered Dirac operator*, *Phys. Rev.* **D78** (2008) 034503, [0804.3929].
- [5] T. G. Kovacs, *Absence of correlations in the qcd dirac spectrum at high temperature*, *Phys. Rev. Lett.* **104** (2010) 031601, [0906.5373].
- [6] T. G. Kovacs and F. Pittler, *Anderson localization in quark-gluon plasma*, *Phys. Rev. Lett.* **105** (2010) 192001, [1006.1205].
- [7] S. M. Nishigaki, M. Giordano, T. G. Kovacs and F. Pittler, *Critical statistics at the mobility edge of QCD Dirac spectra*, *PoS Lattice2013* (2014) 018, [1312.3286].
- [8] T. G. Kovacs and R. A. Vig, *The localization transition in SU(3) gauge theory*, *Phys. Rev.* **D97** (2018) 014502, [1706.03562].
- [9] R. A. Vig and T. G. Kovacs, *Localization transition in SU(3) gauge theory*, *PoS Lattice 2018* (2019) 257, [1811.01887].
- [10] M. Giordano, *Localisation in 2+1 dimensional SU(3) pure gauge theory at finite temperature*, *JHEP* **05** (2019) 204, [1903.04983].
- [11] R. V. Gavai, S. Gupta and R. Lacaze, *Eigenvalues and eigenvectors of the staggered dirac operator at finite temperature*, *Phys. Rev.* **D77** (2008) 114506, [0803.0182].
- [12] T. G. Kovacs and F. Pittler, *Poisson to Random Matrix Transition in the QCD Dirac Spectrum*, *Phys. Rev.* **D86** (2012) 114515, [1208.3475].
- [13] M. Giordano, T. G. Kovacs and F. Pittler, *Universality and the QCD Anderson Transition*, *Phys. Rev. Lett.* **112** (2014) 102002, [1312.1179].
- [14] M. Giordano, S. D. Katz, T. G. Kovacs and F. Pittler, *The chiral transition as an Anderson transition*, *PoS Lattice2014* (2014) 214, [1410.8392].
- [15] M. Giordano, T. Kovacs, F. Pittler, L. Ujfalusi and I. Varga, *Dirac eigenmodes at the qcd anderson transition*, *PoS Lattice2014* (2014) 212, [1410.8308].
- [16] L. Ujfalusi, M. Giordano, F. Pittler, T. G. Kovács and I. Varga, *Anderson transition and multifractals in the spectrum of the Dirac operator of Quantum Chromodynamics at high temperature*, *Phys. Rev.* **D92** (2015) 094513, [1507.02162].
- [17] M. Giordano, *Localisation, chiral symmetry and confinement in QCD and related theories*, *PoS Confinement2018* (2019) 045, [1811.04792].

- [18] M. Giordano and T. G. Kovacs, *Localization of Dirac Fermions in Finite-Temperature Gauge Theory*, Universe **7**, no.6, 194 (2021) [2104.14388 [hep-lat]].
- [19] F. Bruckmann, T. G. Kovacs and S. Schierenberg, *Anderson localization through Polyakov loops: lattice evidence and Random matrix model*, Phys. Rev. **D84** (2011) 034505, [1105.5336].
- [20] G. Cossu and S. Hashimoto, *Anderson Localization in high temperature QCD: background configuration properties and Dirac eigenmodes*, JHEP **06** (2016) 056, [1604.00768].
- [21] L. Holicki, E.-M. Ilgenfritz and L. von Smekal, *The Anderson transition in QCD with $N_f = 2 + 1 + 1$ twisted mass quarks: overlap analysis*, PoS Lattice2018 (2018) 180, [1810.01130].
- [22] G. Baranka and M. Giordano, *Localization of Dirac modes in finite-temperature Z2 gauge theory on the lattice*, Phys. Rev. D **104**, no.5, 054513 (2021) [2104.03779 [hep-lat]].
- [23] M. Giordano, *Localisation of Dirac modes in gauge theories and Goldstone's theorem at finite temperature*, JHEP **12**, 103 (2022) [2206.11109 [hep-th]].
- [24] V. Dick, F. Karsch, E. Laermann, S. Mukherjee and S. Sharma, *Microscopic origin of $U_A(1)$ symmetry violation in the high temperature phase of QCD*, Phys. Rev. D **91**, no.9, 094504 (2015) [1502.06190 [hep-lat]].
- [25] H. T. Ding, S. T. Li, S. Mukherjee, A. Tomiya, X. D. Wang and Y. Zhang, *Correlated Dirac Eigenvalues and Axial Anomaly in Chiral Symmetric QCD*, Phys. Rev. Lett. **126**, no.8, 082001 (2021) [2010.14836 [hep-lat]].
- [26] O. Kaczmarek, L. Mazur and S. Sharma, *Eigenvalue spectra of QCD and the fate of $UA(1)$ breaking towards the chiral limit*, Phys. Rev. D **104**, no.9, 094518 (2021) [2102.06136 [hep-lat]].
- [27] F. Burger, G. Hotzel, M. Mueller-Preussker, E.-M. Ilgenfritz and M. P. Lombardo, *Towards thermodynamics with $N_f = 2 + 1 + 1$ twisted mass quarks*, PoS Lattice2013 (2013) 153, [1311.1631].
- [28] F. Burger, E.-M. Ilgenfritz, M. P. Lombardo, M. Mueller-Preussker and A. Trunin, *Towards the quark-gluon plasma Equation of State with dynamical strange and charm quarks*, J. Phys. Conf. Ser. **668** (2016) 012092, [1510.02262].
- [29] F. Burger, E.-M. Ilgenfritz, M. P. Lombardo, M. Müller-Preussker and A. Trunin, *Topology (and axion's properties) from lattice qcd with a dynamical charm*, Nucl. Phys. **A967** (2017) 880–883, [1705.01847].
- [30] K. Cichy, G. Herdoiza and K. Jansen, *Continuum Limit of Overlap Valence Quarks on a Twisted Mass Sea*, Nucl. Phys. B **847**, 179–196 (2011) [1012.4412 [hep-lat]].
- [31] K. Cichy, V. Drach, E. Garcia-Ramos, G. Herdoiza and K. Jansen, *Overlap valence quarks on a twisted mass sea: a case study for mixed action Lattice QCD*, Nucl. Phys. B **869** (2013), 131–163 [1211.1605 [hep-lat]].
- [32] R. Frezzotti and G. C. Rossi, *Twisted mass lattice QCD with mass nondegenerate quarks*, Nucl. Phys. Proc. Suppl. **128** (2004) 193–202, [hep-lat/0311008].
- [33] F. Burger, E.-M. Ilgenfritz, M. P. Lombardo and A. Trunin, *Chiral observables and topology in hot QCD with two families of quarks*, Phys. Rev. **D98** (2018) 094501, [1805.06001].
- [34] C. Alexandrou, V. Drach, K. Jansen, C. Kallidonis and G. Koutsou, *Baryon spectrum with $N_f = 2 + 1 + 1$ twisted mass fermions*, Phys. Rev. **D90** (2014) 074501, [1406.4310].
- [35] ETM collaboration, R. Baron et al., *Status of ETMC simulations with $N(f) = 2+1+1$ twisted mass fermions*, PoS Lattice2008 (2008) 094, [0810.3807].
- [36] ETM collaboration, R. Baron et al., *First results of ETMC simulations with $N(f) = 2+1+1$ maximally twisted mass fermions*, PoS Lattice2009 (2009) 104, [0911.5244].
- [37] R. Baron et al., *Light hadrons from lattice QCD with light (u,d), strange and charm dynamical quarks*, JHEP **06** (2010) 111, [1004.5284].
- [38] ETM collaboration, R. Baron et al., *Light hadrons from $N_f=2+1+1$ dynamical twisted mass fermions*, PoS Lattice2010 (2010) 123, [1101.0518].
- [39] H. Neuberger, *Exactly massless quarks on the lattice*, Phys. Lett. **B417** (1998) 141–144, [hep-lat/9707022].
- [40] H. Neuberger, *More about exactly massless quarks on the lattice*, Phys. Lett. **B427** (1998) 353–355, [hep-lat/9801031].
- [41] H. Neuberger, *A Practical Implementation of the Overlap Dirac Operator*, Phys. Rev. Lett. **81** (1998) 4060–4062, [hep-lat/9806025].
- [42] H. Neuberger, *An Introduction to lattice chiral fermions, in QCD and numerical analysis III. Proceedings, 3rd International Workshop, Edinburgh, UK, June 30-July 4, 2003*, pp. 3–13, 2003. hep-lat/0311040.
- [43] P. H. Ginsparg and K. G. Wilson, *A Remnant of Chiral Symmetry on the Lattice*, Phys. Rev. **D25** (1982) 2649.
- [44] M. Luscher, *Exact chiral symmetry on the lattice and the Ginsparg-Wilson relation*, Phys. Lett. B **428**, 342–345 (1998) [hep-lat/9802011 [hep-lat]].
- [45] F. Niedermayer, *Exact chiral symmetry, topological charge and related topics*, Nucl. Phys. B Proc. Suppl. **73** (1999) 105–119, [9810026].
- [46] S. Capitani, M. Gockeler, R. Horsley, P. E. L. Rakov and G. Schierholz, *Operator improvement for Ginsparg-Wilson fermions*, Phys. Lett. **B468** (1999) 150–160, [hep-lat/9908029].
- [47] T. Banks and A. Casher, *Chiral Symmetry Breaking in Confining Theories*, Nucl. Phys. **B169** (1980) 103–125.
- [48] T. DeGrand, Z. Liu and S. Schaefer, *Quark condensate in two-flavor QCD*, Phys. Rev. D **74**, 094504 (2006) [erratum: Phys. Rev. D **74**, 099904 (2006)] [hep-lat/0608019].
- [49] H. Fukaya et al. [JLQCD and TWQCD], *Determination of the chiral condensate from QCD Dirac spectrum on the lattice*, Phys. Rev. D **83**, 074501 (2011) [1012.4052 [hep-lat]].
- [50] A. Alexandru and I. Horváth, *Unusual Features of QCD Low-Energy Modes in the Infrared Phase*, Phys. Rev. Lett. **127**, 052303 (2021) [[arXiv:2103.05607 [hep-lat]].
- [51] P. H. Damgaard, U. M. Heller, R. Niclasen and K. Rummukainen, *Low-lying eigenvalues of the qcd dirac operator at finite temperature*, Nucl. Phys. **B583** (2000) 347–367, [hep-lat/0003021].
- [52] V. Hernández, J. E. Román, A. Tomás and V. Vidal, *Krylov-Schur Methods in SLEPc*, (2007).
- [53] J. E. Roman, C. Campos, L. Dalcin, E. Romero and A. Tomás, *SLEPc Users Manual: Scalable Library for Eigenvalue Problem Computations*, (2021).
- [54] D. C. Sorensen, *Implicit Application of Polynomial Filters in a k-Step Arnoldi Method*, SIAM Journal on Matrix Analysis and Applications **13** (1992) 357–385.
- [55] R. B. Lehoucq, D. C. Sorensen, and C. Yang, *APRACK users' guide: Solution of large scale eigenvalue problems with implicitly restarted Arnoldi methods*, (1997).

- [56] F. M. Gomes and D. C. Sorensen, *ARPACK++: An object-oriented version of ARPACK eigenvalue package.*, (2000).
- [57] H. T. Ding and others, *Chiral Phase Transition Temperature in (2+1)-Flavor QCD*, *Phys. Rev. Lett.* **123** (2019) 062002, [1903.04801].
- [58] L. Ujfalusi and I. Varga, *Finite-size scaling and multifractality at the Anderson transition for the three Wigner-Dyson symmetry classes in three dimensions*, *Phys. Rev. B* **91** (May, 2015) 184206, [1501.02147].
- [59] S. N. Evangelou and D. E. Katsanos, *Energy level statistics in disordered metals with an anderson transition*, *Journal of Statistical Physics* **85** (Dec, 1996) 525–550.
- [60] B. Klein and J. J. M. Verbaarschot, *Spectral universality of real chiral random matrix ensembles*, *Nucl. Phys.* **B588** (2000) 483–507, [hep-th/0004119].
- [61] J. J. M. Verbaarschot and T. Wettig, *Random matrix theory and chiral symmetry in QCD*, *Ann. Rev. Nucl. Part. Sci.* **50** (2000) 343–410, [hep-ph/0003017].
- [62] J. Wilhelm, L. Holicki, D. Smith, B. Wellegehausen and L. von Smekal, *Continuum Goldstone spectrum of two-color QCD at finite density with staggered quarks*, *Phys. Rev. D* **100** (2019) 114507, [1910.04495].
- [63] S. Hands, I. Montvay, S. Morrison, M. Oevers, L. Scorzato and J. Skullerud, *Numerical study of dense adjoint matter in two color QCD*, *Eur. Phys. J. C* **17** (2000) 285–302, [hep-lat/0006018].
- [64] B. H. Wellegehausen, A. Maas, A. Wipf and L. von Smekal, *Hadron masses and baryonic scales in G_2 -QCD at finite density*, *Phys. Rev. D* **89** (2014) 056007, [1312.5579].
- [65] A. M. Halasz and J. J. M. Verbaarschot, *Universal fluctuations in spectra of the lattice dirac operator*, *Phys. Rev. Lett.* **74** (1995) 3920–3923, [hep-lat/9501025].
- [66] J. Kogut, D. Toublan and D. Sinclair, *The PseudoGoldstone spectrum of two color QCD at finite density*, *Phys. Rev. D* **68** (2003) 054507, [hep-lat/0305003].
- [67] A. M. Garcia-Garcia and J. C. Osborn, *Chiral phase transition as an Anderson transition in the instanton liquid model for QCD*, *PoS Lattice2005* (2006) 265, [hep-lat/0509118].
- [68] A. M. Garcia-Garcia and J. C. Osborn, *Chiral phase transition and anderson localization in the instanton liquid model for QCD*, *Nucl. Phys.* **A770** (2006) 141–161, [hep-lat/0512025].
- [69] A. M. Garcia-Garcia and J. C. Osborn, *Chiral phase transition in lattice QCD as a metal-insulator transition*, *Phys. Rev.* **D75** (2007) 034503, [hep-lat/0611019].